

## Microstructure of pyrocarbons from pair distribution function analysis using neutron diffraction

Patrick Weisbecker<sup>1\*</sup>, Jean-Marc Leyssale<sup>1</sup>, Henry E. Fischer<sup>2</sup>, Veijo Honkimäki<sup>3</sup>, Maëva Lalanne<sup>1</sup>, Gérard L. Vignoles<sup>4</sup>

<sup>1</sup> CNRS, Laboratoire des Composites ThermoStructuraux, UMR 5801, 3 Allée de la Boétie, F33600 Pessac, France

<sup>2</sup> Institut Laue Langevin, 6 rue Jules Horowitz, BP 156, 38042, Grenoble Cedex 9, France

<sup>3</sup> European Synchrotron Radiation Facility, 6 rue Jules Horowitz, BP 220, 38043 Grenoble Cedex 9, France

<sup>4</sup> Université Bordeaux 1, Laboratoire des Composites ThermoStructuraux, UMR 5801, 3 Allée de la Boétie, F33600 Pessac, France

### Abstract

We present a microstructural investigation of two different pyrocarbons (PyCs), belonging respectively to the rough laminar (RL) and smooth laminar (SL) families. The structure of the materials is analyzed in terms of their pair distribution functions (PDFs) as determined from neutron diffraction experiments. The data are correlated with polarized light optical microscopy, high resolution transmission electron microscopy, Raman microspectrometry, X-ray diffraction, He pycnometry, elastic recoil detection analysis and secondary ion mass spectrometry. Results show that the two materials may be clearly distinguished using the PDF

---

\* Corresponding author

*Email address* : [weisbecker@lcts.u-bordeaux1.fr](mailto:weisbecker@lcts.u-bordeaux1.fr) (Patrick Weisbecker)

data above a 15 Å distance. The PDF of the more ordered carbon (the RL PyC) is also compared to data obtained from an image-guided atomistic reconstruction, showing excellent agreement.

## 1. Introduction

Pyrocarbons (PyCs), and especially low temperature PyCs, are essential constituents of many high performance composite materials. They form the matrices of carbon/carbon (C/C) composites [1] having applications in extremely harsh environments - rocket nozzles and atmospheric re-entry heat shields [2], Tokamak plasma-facing components [3], aeronautic brake discs [4] - as well as the interphases of many ceramic matrix composites like the SiC/SiC materials envisaged for fuel cells of fourth generation nuclear plants or future nuclear fusion reactors [5]. Both PyC matrices and interphases are usually deposited on a fibrous preform by gas pyrolysis and chemical vapor deposition (CVD) or infiltration (CVI) [6].

In the pyrocarbons the arrangement of carbon atoms is principally based on stacks of graphene layers, faulted to some extent: turbostratic arrangement, non-sp<sup>2</sup> carbon atoms, 5- or 7-membered rings, local curvatures, etc [7-8]. In relation with this, they can contain up to 5 atomic percent of hydrogen, according to elastic recoil detection analysis (ERDA) measurements [9]. These defects strongly impact the properties of the materials and two classes of low temperature PyCs, the rough laminar (RL) and smooth laminar (SL) PyCs, have first been identified by Lieberman and Pierson [10], based on their different optical extinction angle values in polarized light optical microscopy (PLOM) – *i.e.*, the angle between crossed polarizer and analyzer above which the “maltese cross” of a PyC deposited on a fiber disappears. Other PyC classes have then been obtained in the following years by changing the carbon precursors or the synthesis conditions (the gas residence time being the most crucial one [11-12]). They display a large range of degree of anisotropy, which correlates to critical properties, like their ability to graphitize upon high temperature treatments [13].

The structure of those PyCs – in the common sense meaning – has been studied by many groups, using many experimental apparatuses. Special attention has been paid to transmission electron microscopy (TEM) and derived techniques like high resolution TEM (HRTEM), electron energy loss spectroscopy (EELS) or selected area electron diffraction (SAED). HRTEM imaging allows observing the  $002$  lattice fringes, which are more or less wavy from one PyC to another and shows the extent of the coherent stacks of graphene layers. Parameters such as the length of a perfect fringe, the length of a distorted fringe and the number of fringes in a stack can be extracted from the images [14-15], but with a limited accuracy. SAED patterns give a measure of the disorientation of the graphene stacks through the determination of the opening angle ( $OA$ ) corresponding to the width of the  $002$  arc [15-18]. From  $OA$  values a classification has been created -- highly textured (HT), medium textured (MT), and low textured (LT) correspond respectively to low, medium and high values of  $OA$ . This criterion is in good correlation with the PLOM extinction angle values [18]. The diameter and thickness of the coherent domains ( $L_a$  and  $L_c$  respectively) can be determined through the full width at half maximum ( $FWHM$ ) of the diffraction peaks and the interlayer spacing  $d_{002}$  is obtained from the position of the  $002$  peak [15,19].

Raman spectroscopy is also a particularly interesting technique to investigate the structure of carbons as it is both sensitive to low energy defects [20-21] and to the local anisotropy of the material [22]. Using Raman spectroscopy, Bourrat *et al.* [23] have proposed a two-dimensional classification of PyCs based on two Raman observables: the full width at half maximum of the Raman D band ( $FWHM_D$ ), sensitive to the amount of defects in the material; and an anisotropy parameter, the Raman anisotropy factor ( $R_A$ ) defined as the ratio of the Raman intensity measured with the polarizer alone on the intensity measured with an analyzer in cross position. The low temperature PyC family has been split into five classes: rough laminar (RL), smooth laminar (SL), regenerated laminar (ReL), dark laminar (DL) and

granular (G). Figure 3 shows such a diagram with the five PyC families indicated by rectangles. As can be seen, RL PyCs are very anisotropic and contain very little amounts of defects. G PyCs are also low defects carbons but are much less anisotropic than RL PyCs. SL PyCs have a similar anisotropy as G PyCs but show more defects while DL PyCs have the same amount of defects as SL PyCs but are even less anisotropic than the latter. Finally, ReL PyCs have the same anisotropy as RL PyCs while being the most defect-containing family of the classification. They have long been confused with RL PyC because they have similar anisotropy, however, their PLOM appearance is distinct [24], and are not distinguished between each other in the HT/MT/LT classification [18].

Connecting this classification with the study of the influence of the gas phase maturation on the nanotexture of PyCs [11] has showed [21] that RL PyCs result from a heterogeneous growth mechanism of light hydrocarbons at short residence times while ReL PyCs are formed through homogeneous nucleation of large aromatic hydrocarbons at long residence times. Other PyCs of the classification are obtained from heterogeneous mechanisms at intermediate residence times, except G PyC, which appears as a transient layer before RL PyC deposition.

X-Ray or Neutron scattering is another particularly interesting tool to investigate the structure of carbons [19,25-27] as it allows for an accurate quantitative determination of structural parameters like  $d_{002}$ ,  $L_c$  and  $L_a$  from the diffraction data [19,28-29]. In addition to the Bragg peaks, information contained in the diffuse scattering of the pattern are particularly valuable as they contain the atomic structure factor  $S(Q)$  whose Fourier transform, the pair distribution function (PDF), is directly a measure of the distribution of interatomic distances in the material [30]. The first reported PDFs of carbon materials date from the earlier work of Warren [31] and Franklin [32] on carbon blacks. More recently this technique has been applied to various nanoporous carbons obtained by pyrolysis of precursors like poly(furfuryl alcohol) [33], epoxy Novolac [34] or polyparaphenylene [35] resins, anthracene [36-37],

saccharose [36-38]. Activated [39] or carbide derived [40] carbons as well as nanocarbons like, for instance, MWCNTs [41-42] have also been studied with those techniques. Also,  $S(Q)$  or PDFs can be obtained from electron diffraction techniques as done by O'Malley *et al.* [43] and Petersen *et al.* [44] for respectively a glassy carbon and an industrial char. This regain of interest on the PDF determination is partly due to the development of atomistic reconstruction methods, like the reverse Monte Carlo (RMC) method [45] or derived techniques, allowing to build accurate atomistic models of materials from the knowledge of their PDF. Indeed, many atomistic models of various kinds of carbons have been built in the past years from experimental structure factors or PDFs [39-40, 43-44, 46-48].

However, neither any structure factor nor any PDF has ever been reported experimentally so far for pyrocarbons to our knowledge. This is due to the fact that PyCs are frequently obtained under the form of thin deposits on a fibrous textile while an  $S(Q)$  or PDF determination requires a powder obtained from a pure bulk sample. Indeed, up to now, only a few diffraction (X-Ray) studies on C/C composites have been reported, the structural information ( $d_{002}$ ,  $L_a$  and  $L_c$ ) related to the PyC matrix being obtained by subtracting the signal of the fibrous preform from the total diffraction pattern [22, 24].

In this work we have applied a synthesis methodology allowing the preparation of bulk samples of SL and RL PyCs from CVI experiments. These samples have then been grounded and their PDF determined using Neutron diffraction. Samples preparation and details of the different techniques used to characterize them are described in section 2. In section 3 we present the structural features of these two PyCs, including their  $S(Q)$  and PDF as obtained from Neutron diffraction experiments. Finally, the results are discussed in section 4 where we also compare the PDF of the RL PyC to the one of an atomistic model reconstructed by

Leyssale *et al.* on the basis of a HRTEM lattice fringe image [49].

## 2. Experimental

### 2.1 Sample preparation

Rough laminar pyrocarbons (RL) are usually obtained by infiltration of a gaseous precursor through a porous preform made of carbon fibers, making difficult the separation of the PyC from the preform. As the PDF determination requires the material to be in a bulk form, we propose here a special procedure, schematized on Figure 1a, to obtain bulk RL PyC. To do so, fused quartz tubes are filled at both ends with a 3D Novoltex® carbon fiber preform. In order to avoid gas leakage in possible voids located between the tube and the preform, the interface is filled with a carbon cement (C34 cement powder and resin from GrafTech heat) before the tube undergoes a two hours heat treatment at 100°C to cure the cement.

Such a sealed tube has been placed in an isothermal isobaric CVI (I-CVI) reactor with a methane/propane mixture as carbon precursor, and deposition was performed for more than a week to obtain a sufficient amount of PyC ( $\approx 100$  mg). More details on the I-CVI conditions can be found in former work [6]. Finally, two empty tubes were also placed in the furnace to deposit SL PyC.

Pictures of the PyC foils obtained in the sealed tube (after cutting with a diamond saw) and unsealed tubes, at the end of the deposition process, are respectively shown on Figures 1b and 1c. In what follows, PyC-1 will designate the pyrocarbon deposited in the sealed tube (Figure 1b) and PyC-2 the one from the empty tubes (Figure 1c). All the characterizations reported in this paper have been obtained from these PyC samples, resulting from a single synthesis run.

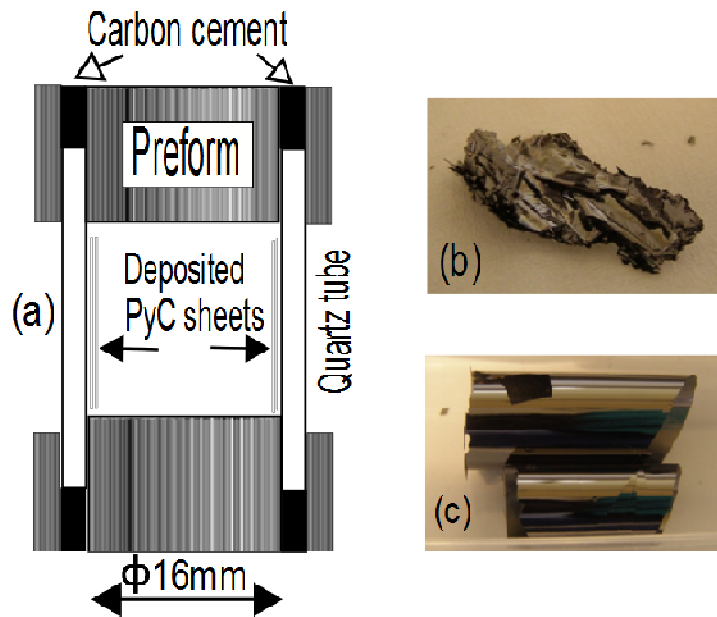


Figure 1: Schematic drawing of the infiltration cell (a) and pictures of the PyC foils obtained by infiltration inside the sealed tube (PyC-1) (b) and by deposition inside the empty tube (PyC-2) (c).

## 2.2 Characterization

Density measurements are performed using a Micromeritics 1340 He pycnometer after cleaning the samples in ethanol and baking them at  $100^{\circ}\text{C}$  during 1h to remove the solvent. The hydrogen content of the different deposits is determined by elastic recoil detection analysis (ERDA) using a  $2.2\text{MeV } 4\text{He}^{+}$  beam and secondary ion mass spectrometry (SIMS) using a  $\text{Cs}^{+}$  ion beam accelerated at 1kV. ERDA analysis allows a quantification of the absolute hydrogen concentration, however this analysis require a perfectly flat surface,  $7 \times 7 \text{ mm}^2$  wide, preventing PyC-1 to be analyzed using this technique. Thus PyC-2 is analyzed

using both techniques and the H content determined by ERDA is used to calibrate the SIMS analysis for PyC-1.

The samples are embedded in a G1 epoxy resin and pressed between a 500 $\mu\text{m}$  thick silicon wafer and a 150 $\mu\text{m}$  thick glass slide, before curing the epoxy resin at 100°C for 20 minutes. Then, several slices with a 700 $\mu\text{m}$  thickness are cut from the “sandwich” using a diamond wire saw and polished in cross section using a Minimet® polisher for polarized light optical microscopy (PLOM) observations and Raman characterizations. Extinction angle ( $A_E$ ) values are measured with a NIKON ECLIPSE microscope mounted with a  $\times 50$  objective and a Xenon halogen light source. Raman analysis are performed with a Labram HR (Jobin Yvon) microspectrometer ( $\lambda = 632.8 \text{ nm}$ ).

Prior to TEM observations, slices thicknesses are reduced to 120 $\mu\text{m}$  by mechanical polishing using a 15 $\mu\text{m}$  diamond plate. The JEOL Ion Slicer (EM-09100IS) device is used for Ar<sup>+</sup> ion milling, performed using an incident energy of 6 keV and an incident angle of 0.5° for 2 hours. The incident angle is then increased to 2.4° and the milling carried on during 1 hour until perforation occurs in the specimen. Thin slices are then decontaminated at 2 keV and 4° incidence.

TEM analyses are carried out with a Philips CM30ST TEM (LaB<sub>6</sub> operated at 300 kV) with a point resolution of 0.2 nm and an information limit of 0.12 nm. Conventional bright field (BF) and (002) dark field (DF) images as well as selected area electron diffraction (SAED) patterns, with a selected area of 400 nm diameter, are acquired on the samples. In parallel, high-resolution transmission electron microscopy (HRTEM) images are obtained on the thinner parts of the thin slices.

Raw PyC foils are powdered prior to the neutron and X-ray experiments. Dry ball milling with a Retsch MM200 miller (5 mm stainless steel balls and 5 ml jars) is used to reduce the granulometry to roughly 10  $\mu\text{m}$  in ten minutes; a short enough time to avoid damaging the structures. After milling, the iron pollution coming from the jars and balls is dissolved in hydrochloric acid at room temperature for one hour. Powders are eventually recovered by filtration through a Durapore® PVDF membrane, washed with ethanol and baked at 100°C during one hour.

Synchrotron diffraction measurements were carried out on beam line ID15B at the European Synchrotron Radiation Facility (ESRF). Samples were placed in a 2.5 mm diameter silica capillary and the scattered intensity measured using a large area detector (Pixium 4700 detector) using X-rays of 87 keV ( $\lambda = 0.14 \text{ \AA}$ ); the contribution of the capillary was subtracted later on from the X-ray pattern.

A conventional approach (including Lorentz polarization and atomic scattering factors corrections) [50] has been used to determine (i) the apparent mean dimension of the carbon stack along the  $c$  axis  $L_c$ , derived from the full width at half maximum of the  $002$  reflection using the Scherrer formula, (ii) the average distance  $d_{002}$  between the aromatic layers and (iii) the in-plane layer dimension  $La_{10}$  calculated from the  $FWHM$  of the  $10$  band [19].

Data were obtained after fitting the  $002$  peak, the  $10$  band and the  $004$  peak with split pseudo Voigt functions using the Topas® software [51]. Peaks were corrected for the instrumental broadening (determined from the Fe standard used for the wavelength determination).

We performed the Neutron diffraction measurements on the D4 diffractometer at the Institut Laue-Langevin (ILL) [52]. Cylindrical vanadium containers of 5mm diameter were filled with the powders and the vertical slits were set to 4 mm horizontal opening, ensuring a constant

sample height in the beam, regardless of the sample. It must be underlined that PyC foils tend to orientate normally to the container axis when the latter is filled vertically, leading to a decrease of  $00l$  peaks. The only way we found to fill the containers without preferential orientations of the foils was to fill them horizontally with a spatula and to avoid unnecessary shaking and packing of the powders. Total scattered intensities were measured as a function of the scattering angle  $2\theta$  for an incident neutron wavelength of  $0.4970 \text{ \AA}$  determined using a Nickel sample. The  $2\theta$  scan range was  $1.54^\circ$ - $137.8^\circ$  with a step of  $0.125^\circ$  corresponding to a scattering vector  $Q$  in the range  $0.34$ - $23.6 \text{ \AA}^{-1}$ . The samples' scattered intensities were obtained from the raw data by subtracting the empty container scan and the empty belljar scan, taking into account corrections for multiple-scattering and attenuation. PDFs of the two PyCs were then obtained using the standard procedure: Placzek correction and Fourier transform (details of the PDF measurement technique can be found in [30] and [53]).

### 3. Results and discussion

#### 3.1 Helium pycnometry

The main characterization results of the two materials are summarized in Table 1 and we start by discussing their densities as determined from He pycnometry. As can be seen on this table, the measured densities of PyC-1 and PyC-2 are respectively of 2.12 and 1.93 g/cm<sup>3</sup>. These values are consistent with those reported by various authors [10, 14, 17, 22, 24] for RL and SL PyCs respectively. For instance Bourrat *et al.* give mean values of respectively 2.13 and 1.95 g/cm<sup>3</sup> for RL and SL PyCs [24].

Table 1: Summary of the structural parameters for PyC-1 and PyC-2.  $d_{002}$ ,  $L_c$  and  $La_{10}$  are structural parameters obtained from X-ray diffraction;  $A_E$  is the extinction angle from polarized light optical microscopy;  $R_A$  and  $FWHMD$  are respectively the Raman anisotropy factor [22] and the full width at half maximum of the Raman D band;  $d$  is the density as measured from He pycnometry and % *at. H* is the atomic percent of Hydrogen as obtained from ERDA/SIMS (see text) measurements.

Sample	$d_{002}$ (Å)	$L_c$ (nm)	$La_{10}$ (nm)	$A_E$ (°)	$R_A$ (-)	$FWHMD$ (cm <sup>-1</sup> )	$d$ (g/cm <sup>3</sup> )	% <i>at. H</i> (%)
PyC-1	3.436±0.003	4.1±0.1	4.6±0.3	25±2	8.2±0.5	83±2	2.12±0.01	0.7±0.4
PyC-2	3.448±0.003	2.6±0.1	3.3±0.3	10.5±0.3	5.5±0.5	109±2	1.93±0.01	1.1±0.2

### 3.2 Polarized light optical microscopy

Figure 2 shows PLOM images of PyC-1 (Fig. 2a) and PyC-2 (Fig. 2b) samples. PyC-1 is made of at least eight well-separated foils with thicknesses ranging from 1 to 6  $\mu\text{m}$  while PyC-2 is a massive unique foil, 30  $\mu\text{m}$  thick. As can be seen on Figure 2b, PyC-2 appears to be extremely homogeneous when observed by PLOM and no growth cones can be detected (some weak columnar contrasts crossing the foil were observed, but can be hardly seen on the image). This is a very typical feature of SL PyCs [14]. On the opposite, PyC-1 shows a very pronounced columnar texture, indicative of a large amount of growth cones, a well-known property of RL PyCs [14, 20]. Extinction angles of  $25^\circ \pm 2^\circ$  for PyC-1 and  $10.5^\circ \pm 0.5^\circ$  for PyC-2 are respectively typical of RL ( $19^\circ$ - $20^\circ$  according to Vallerot *et al.* [22]) and SL ( $10^\circ$ - $11^\circ$  in [22]) PyCs.

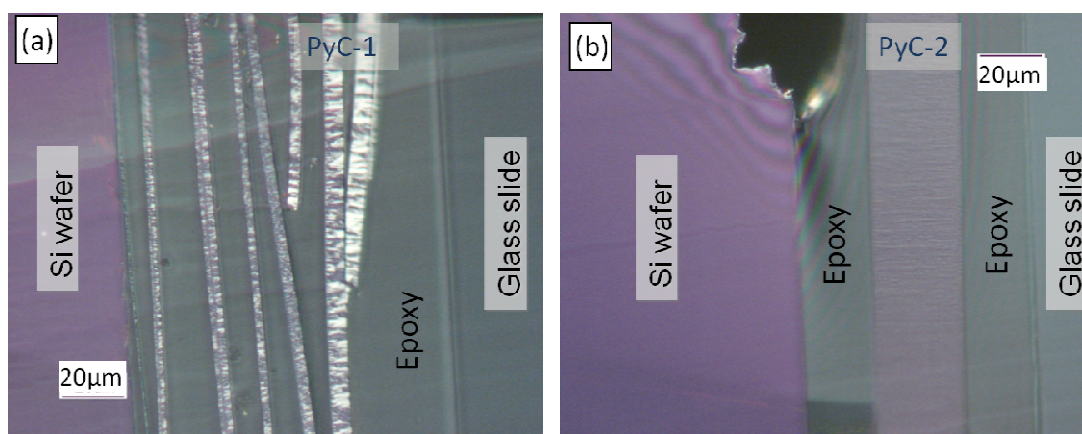


Figure 2. PLOM images of PyC-1 (a) and PyC-2(b) samples

### 3.3 X-Ray diffraction

X-Ray diffraction data are also given in Table 1. The  $d_{002}$  values of 3.436  $\text{\AA}$  for PyC-1 and 3.448  $\text{\AA}$  for PyC-2 correspond to the interlayer spacing usually admitted for a pure turbostratic carbon [28, 54]. The difference in interlayer spacing between the two PyCs is not significant. Also, PyC-2 has a much lower value of  $L_c$  (2.6 nm) than PyC-1 (4.1 nm), which

could in-turn explain the small difference in the measured  $d_{002}$  values for these two materials. Indeed, Fujimoto [55] and Li *et al.* [56] have underlined that the  $002$  peak shifts toward lower angles when  $L_c$  decreases, independently of the “real”  $d_{002}$  value.

Taking into account those values of  $d_{002}$  and  $L_c$ , PyC-1 and PyC-2 seem to be made of crystallites containing stacks of respectively 12 and 8 graphene layers. The difference between the in-plane layer dimension,  $L_{a10}$ , of the two PyCs, 4.6 nm for PyC-1 and 3.3 nm for PyC-2, is also significant enough to show that PyC-1 has larger crystallites than PyC-2, although the strong overlap between the highly asymmetric  $10$  band and the  $004$  peak leads to strong uncertainties in the determination of  $L_a$  values. It should be kept in mind that  $L_c$  and  $L_a$  do not really give us the dimensions of crystallites, as the structure of the materials under investigation here is much more complex than a simple turbostratic stacking of graphitic layers. However those values allow for a comparison of the materials considered here with the data published by others on similar carbons [24]. Also, considering an oversimplified model of cylindrical crystallites of diameter  $L_a$ , height  $L_c$  and interplanar distance  $d_{002}$ , gives crystallites of 7656 and 2668 atoms for respectively PyC-1 and PyC-2.

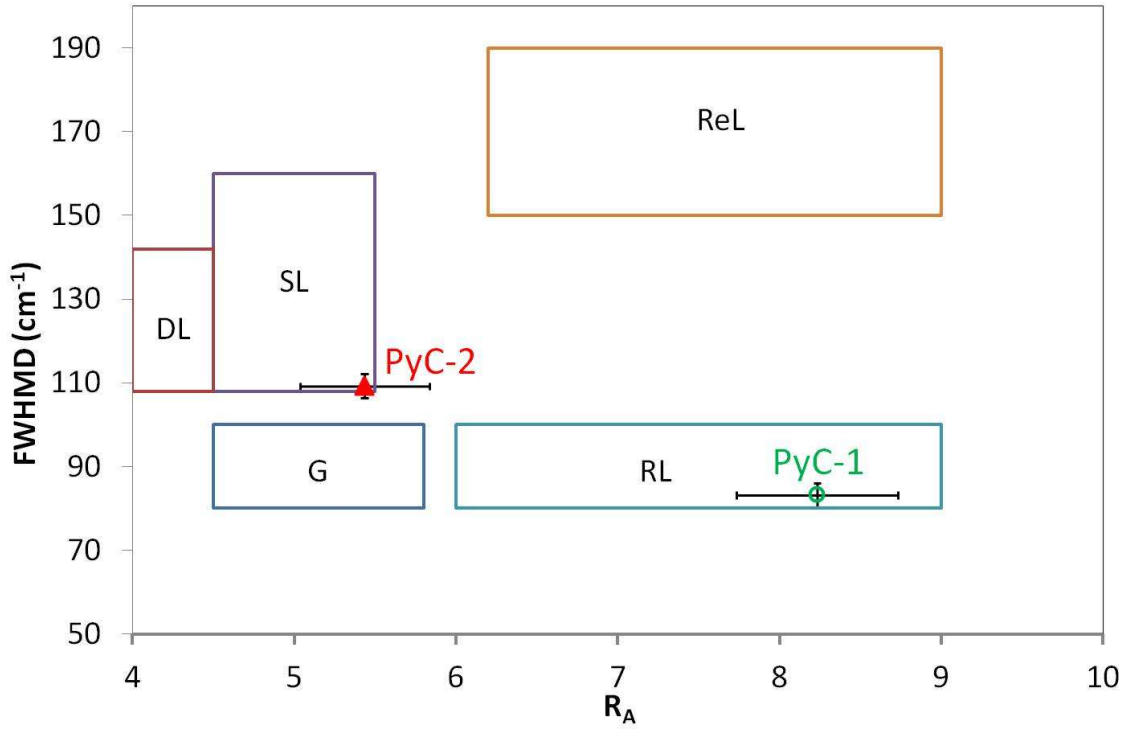


Figure 3: Location of PyC-1 (circle) and PyC-2 (triangle) samples on the Raman based 2D classification proposed by Bourrat *et al.* [23].  $R_A$  is the anisotropy ratio;  $FWHM_D$  is the full width at half maximum of the Raman D band; Error bars correspond to the standard deviation of our measurements (around 10 measurements performed for each PyC, distant of at least a few mm on PyC-2 and including different foils for PyC-1). Indicated with rectangles are the existence domains of the five main low temperature PyC classes: dark laminar (DL), rough laminar (RL), regenerative laminar (ReL), granular (G) and smooth laminar (SL).

### 3.4 Raman microspectrometry

Figure 3 shows the positions of PyC-1 and PyC-2 on the 2D classification. With  $R_A = 8.2$  and  $FWHM_D = 83 \text{ cm}^{-1}$ , PyC-1 definitely belongs to the RL PyC family. PyC-2, on the other hand, with  $R_A = 5.5$  and  $FWHM_D = 109 \text{ cm}^{-1}$  is a SL PyC. In both cases, the carbons synthesized in this work are located at the high anisotropy/low defect corner of their respective families.

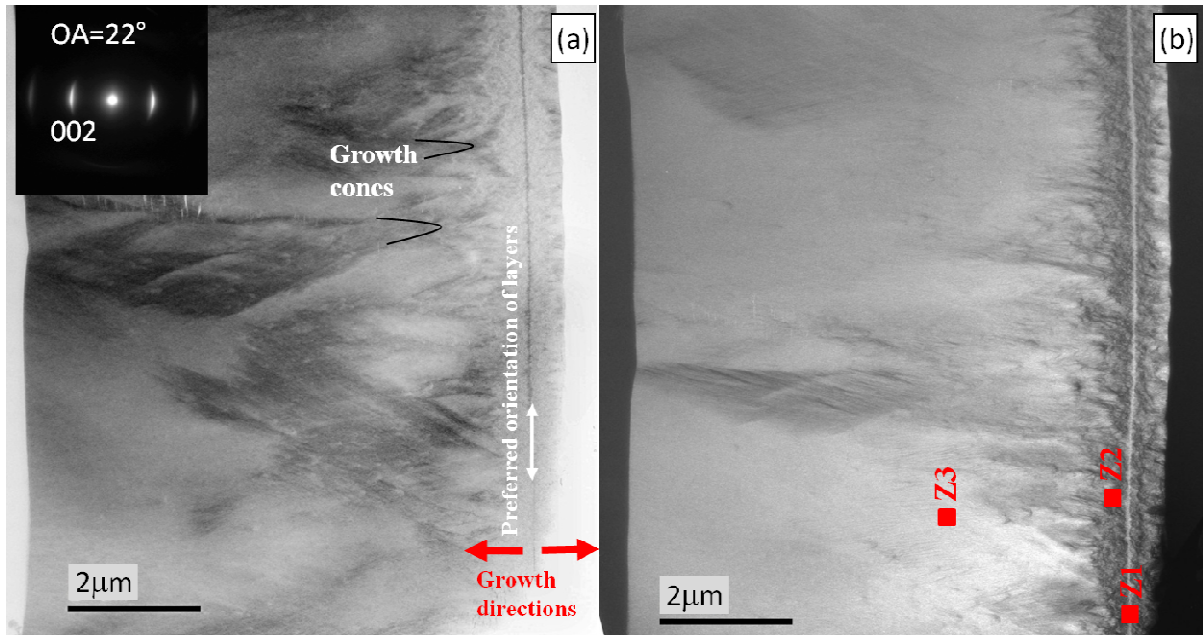


Figure 4: Cross-section TEM images of PyC-1 in bright field (a) and (002) dark field (b) modes. Two growth cones, as well as the preferred orientation of layers in zones Z1 and Z3 and the growth direction are highlighted with respectively black lines, white arrows and red arrows on panel (a). The SAED pattern corresponding to a growth cone is given as an inset to panel (a). Red squares on panel (b) indicate the locations of three regions observed in HRTEM mode (see Figure 5).

### 3.5 Transmission electron microscopy

Figure 4 shows the cross section TEM images of a foil of PyC-1 in bright (Fig. 4a) and (002) dark (Fig. 4b) field modes. As can be seen, the foil is made of three distinct zones, noted Z1 to Z3 in what follows. Z1 appears as a dark (respectively light) vertical thin (50 nm) line on Fig. 4a (resp. Fig. 4b). It is surrounded on both sides by a 400 nm domain, Z2, appearing respectively light and dark on Figs 4a and 4b. Finally, Z3 (respectively dark on Fig 4a and light on Fig. 4b) develops on both sides although being much thicker on the left side of the

foil (around 6  $\mu\text{m}$ ) than on the right side (around 100 nm). These observations seem to show that Z1 and Z3 correspond to anisotropic carbon with graphene sheets preferentially ordered parallel to the foil surface (as indicated by the white arrows on Fig. 4a). This is both confirmed by the observation of growth cones on Z3 and by the anisotropic SAED pattern taken in one of those cones. On the contrary, Z2 looks much less anisotropic.

Figure 5 shows HRTEM lattice fringe images taken on Z1, Z2 and Z3 domains. They clearly confirm the highly anisotropic nature of Z1 and Z3 as well as the very disordered nature of Z2. Z3, the main constituent of our PyC-1 foil, is composed of slightly curved extended graphene layers, packed tightly together and with a high degree of alignment, in close agreement with the nanotexture of RL PyCs (see also its opening angle  $OA$  of  $22^\circ$  as measured from the SAED pattern of Fig 4) [14, 22]. Z1 is also a very organized anisotropic PyC although some of the fringes show some important curvatures. Finally, Z2 corresponds to a very disordered carbon, typical of the low anisotropy PyC families (SL, G, DL).

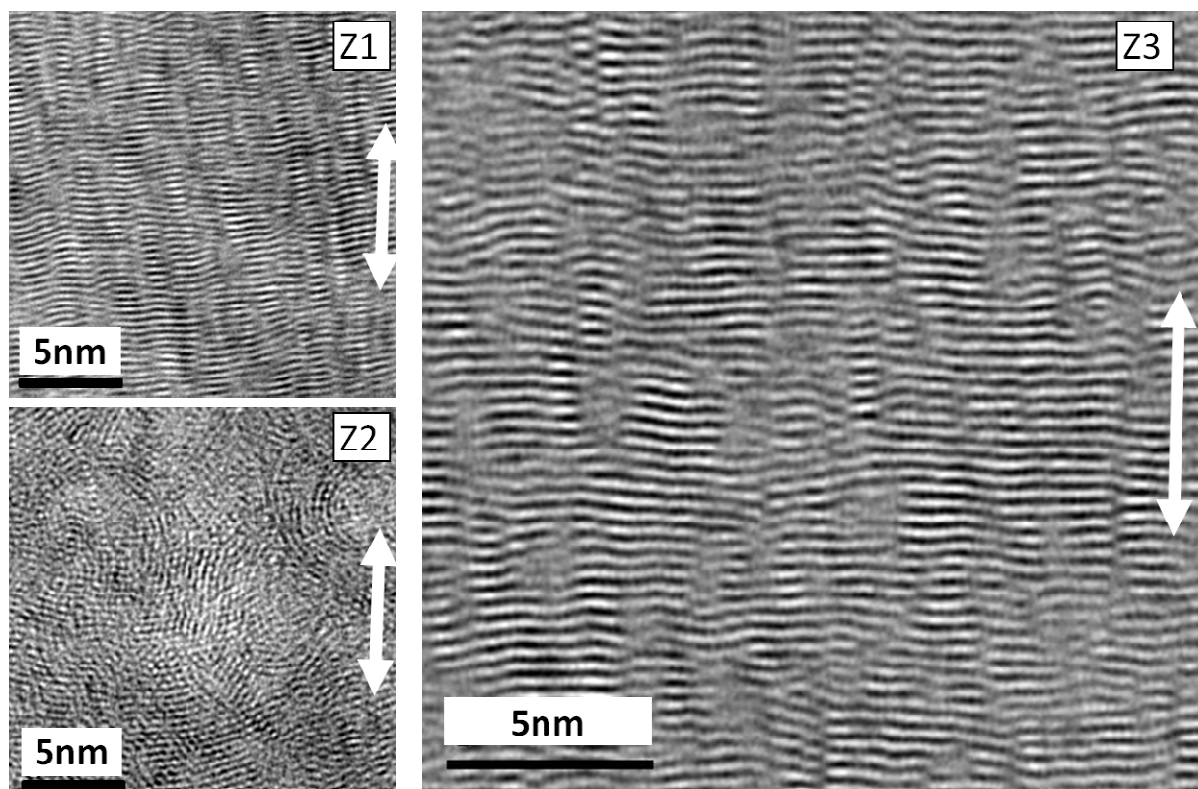


Figure 5: HRTEM images of Z1, Z2 and Z3 domains of PyC-1. Images Z1 and Z3 have been filtered using the average background subtracted filter (ABSF) [57-58]. The arrows indicate the growth direction.

This microstructure is in agreement with previous observations [12, 17, 59-60]. In an interesting paper Chen *et al.* [60] describe the microstructure of a carbon matrix deposited on a carbon preform as a successive arrangement, along the deposition process, of a high-textured (HT) carbon layer, debonded from the fiber, a medium-textured (MT) layer and eventually, the high-textured bulk layer. Bearing this in mind, we can hypothesize that Z1 could be the first carbon deposited during the CVI process on the surface of the fused quartz tube. Then, due to weak adhesive interactions between this layer and the tube, and to possible stresses in the carbon, this layer could peel off from the tube and offer two surfaces to the gas for deposition. Following this, a disordered layer (Z2) could start growing on both sides of this thin foil and be followed by the deposition of a high-textured (RL) thick layer (Z3).

In their paper, Chen et al. [60] do not conclude definitively on whether the thin high-textured carbon layer present at the fiber/matrix interface results from the deposition process or from a modification of the fiber surface. Our work unambiguously shows that it comes from the gas. We add that such a microstructure was observed in every foil of PyC-1, although the location of Z1 can vary from a very central position to a very asymmetric one (see Fig. 4) from one foil to another.

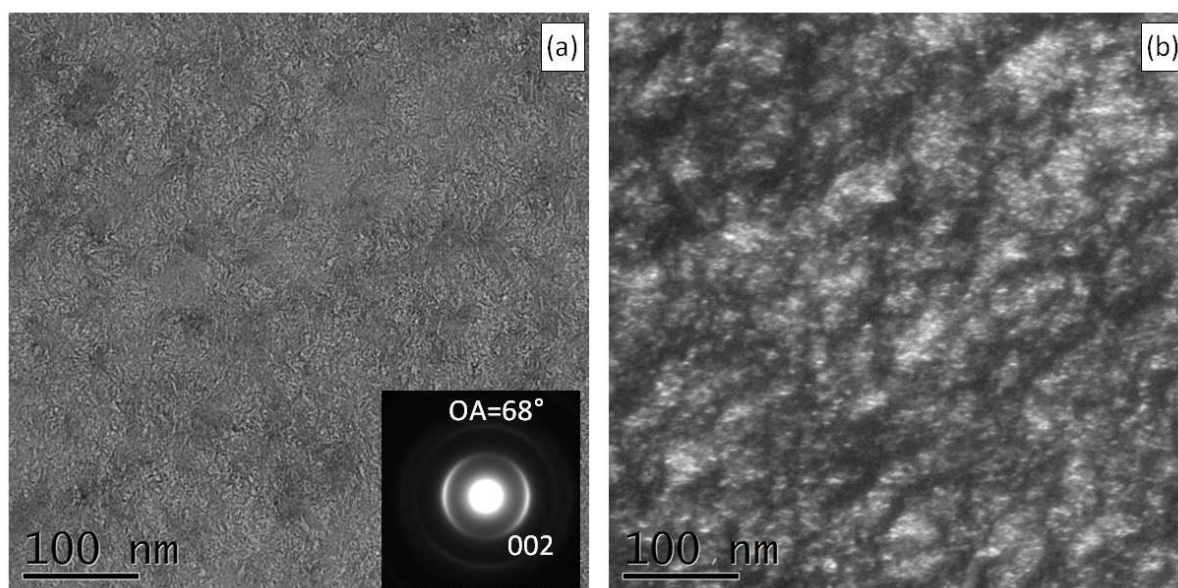


Figure 6: Cross-section TEM images of a PyC-2 foil in bright field (a) and (002) dark field (b) modes. A corresponding SAED pattern is shown as an inset to panel (a).

Figure 6 shows cross section TEM images and a SAED pattern of PyC-2. It is homogeneous on the whole thickness of the sheet (30 $\mu$ m). Small domains of roughly 30 to 50 nm are observed in the bright (Fig. 6a) and dark (Fig. 6b) field images. In these domains the graphene layers have a common average orientation. The SAED pattern (Fig. 6a), taken on a 400 nm domain, and the corresponding  $OA$  value of 68 $^\circ$  confirm that this is a medium-textured carbon according to the classification given by Reznik *et al.* [17]; this  $OA$  value is also consistent with a smooth laminar (SL) pyrocarbon as defined by Bourrat *et al.* [23]. The HRTEM image

of Figure 7 shows that the deposit is composed of wavy graphene layers, with strong distortions and curvatures. They form large pseudo-coherent domains with a global orientation of the fringes parallel to the foil surface and some smaller domains with random orientations. Nevertheless, really coherent patterns, i.e. the basic structural units (BSU) [16], do not exceed a few nanometers. All these features are typical of SL PyCs [14, 24].

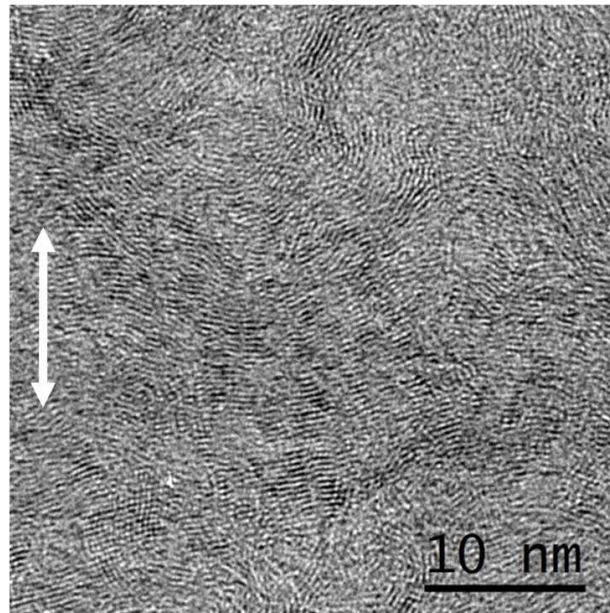


Figure 7: HRTEM image of PyC-2. The arrow indicates the growth direction.

### *3.6 Hydrogen content*

According to our ERDA and SIMS measurements, PyC-1 and PyC-2 contain respectively around 0.7 and 1.1 atomic percent of hydrogen. This is in contradiction with former results (up to 6% at.) on similar carbons, as obtained by ERDA [9]. However, some authors [61] have noted that pyrocarbons, after preparation, may contain an appreciable amount of trapped hydrogen, which can be degassed in certain conditions (e.g. high-temperature argon flow after

deposition). Differences in the thermal history of the samples could also result in apparently contradicting results.

### *3.7 Neutron diffraction*

The structure factors of PyC-1 and PyC-2, as obtained from neutron diffraction are shown on Figure 8. Reproducibility tests were performed with other PyC samples (not presented in this paper for conciseness) – an SL sample with properties similar to PyC-2 (same values of  $FWHM_D$ ,  $R_A$ ,  $A_E$  and density) and an RL sample, with similar  $FWHM_D$ ,  $R_A$ ,  $A_E$  and a slightly higher density than PyC-1. The differences between structure factors of two materials belonging to the same family was always negligible with respect to the differences in  $S(Q)$  between an RL and an SL PyC. As can be seen, the two carbons have extremely similar  $S(Q)$  functions and almost no distinction can be made between them for  $Q$  values larger than  $6 \text{ \AA}^{-1}$  (i.e. after the  $11$  peak at  $Q = 5.15 \text{ \AA}^{-1}$ ). Below that value, neatly visible peaks corresponding to  $002$  and  $004$  reflections and  $10$  and  $11$  bands are found at the same locations for both PyCs but with a lower width for PyC-1 than for PyC-2. This is particularly the case for the  $002$  and  $004$  reflections, and this is consistent with  $L_c$  values obtained in the synchrotron experiments. Nevertheless, more information – usually not taken into account when dealing only with  $d_{002}$ ,  $L_a$  and  $L_c$  - can be obtained from an analysis using the whole  $Q$  range.

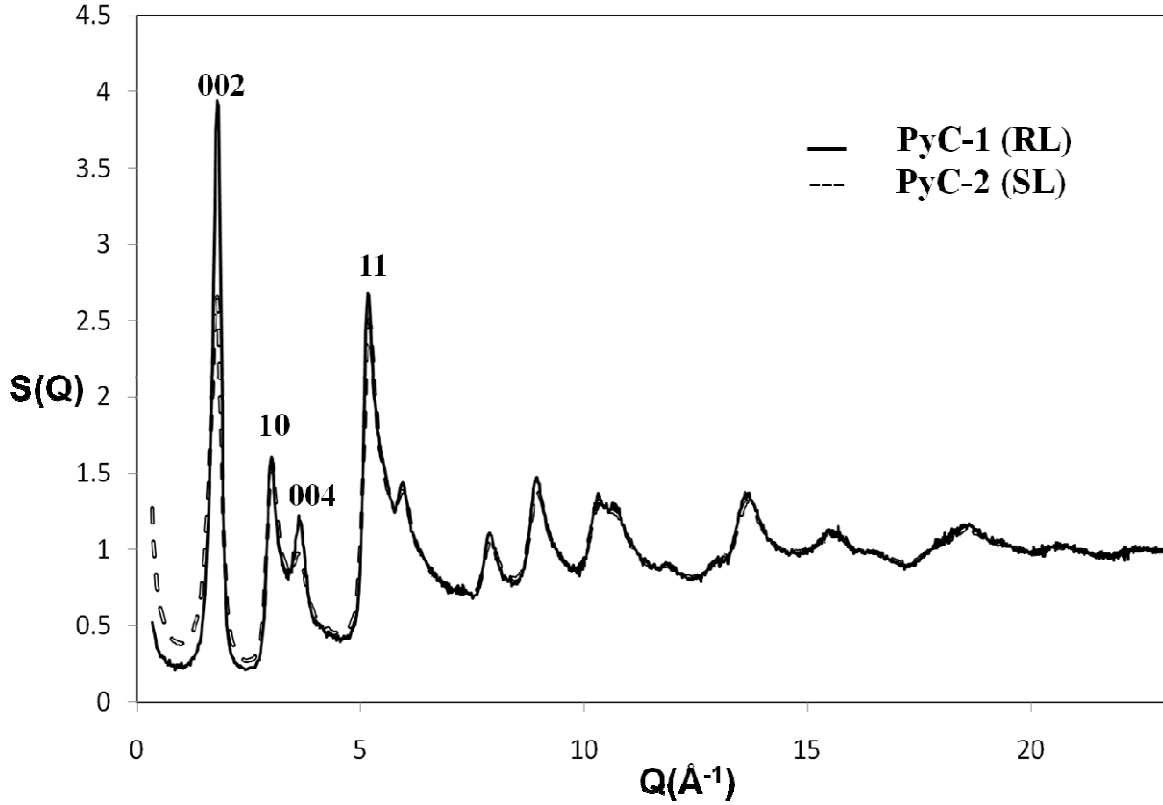


Figure 8: Structure factors  $S(Q)$  of PyC-1 (solid line) and PyC-2 (dashed line) (Neutron D4 data).

The reduced pair distribution functions,  $G(r)$ , easily obtained from the total scattering structure factor  $S(Q)$  by [30]:

$$G(r) = \frac{2}{\pi} \int_0^{\infty} Q[S(Q) - 1] \sin Qr \, dQ, \quad (1)$$

are shown on Figures 9a and 9b for respectively PyC-1 and PyC-2. Oscillations of  $G(r)$  before the first peak at 1.42 Å are artifacts due to the finite maximum accessible value of  $Q$  (this is also responsible for peak broadening after the Fourier transform [53]). PDFs of both PyCs have extremely similar aspects and present the same peaks at the same locations. The short-range structure is similar to the one of graphite: the first three peaks are positioned at real space distances of 1.42, 2.46 and 2.83 Å, matching the in-plane  $C-C$  bond distances in graphite (1.43 Å, 2.46 Å and 2.85 Å). The difference between the two functions lies essentially in the quicker decrease of  $G(r)$  intensity with interatomic distance  $r$  for PyC-2 than for PyC-1.

This is related to the shorter range of structural coherence in both the stacking and lateral extension of the graphene sheets in the smooth laminar sample (PyC-2).

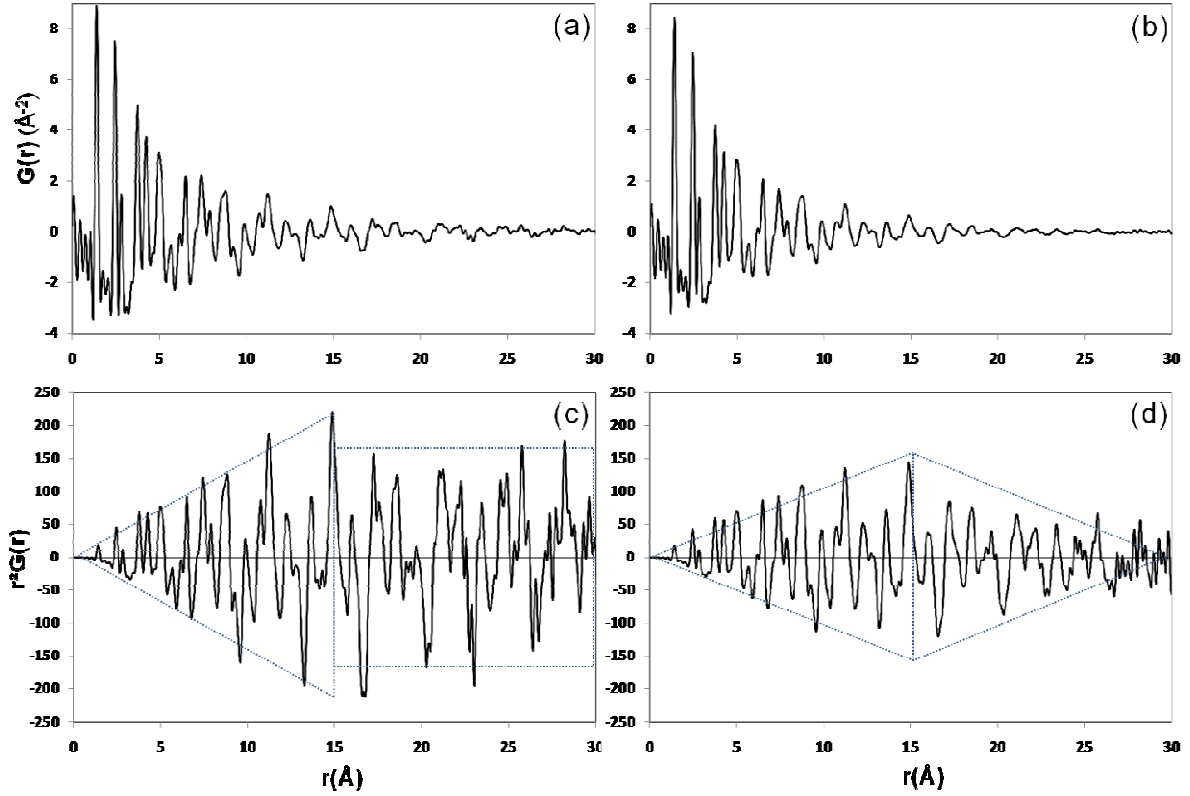


Figure 9: Reduced pair distribution functions  $G(r)$  of PyC-1 (a) and PyC-2 (b) and  $r^2G(r)$  data for PyC-1 (c) and PyC-2 (d); the dashed left arrow (c) and lozenge (d) indicates the shape of the envelope of  $r^2G(r)$  data. (Neutron D4 data).

The plots of  $r^2G(r)$  data for PyC-1 (Fig. 9c) and PyC-2 (Fig. 9d) allow investigating this point a bit further. As can be seen, when going from  $r = 0$  to  $r = 15 \text{ \AA}$ , peaks of increasing intensity are regularly found (following a left arrow shaped envelope) for PyC-1 and the maximum intensity (around -200 and +200) peaks are found at  $r \approx 15 \text{ \AA}$ . Above that distance, and up to the largest  $r$  values accessible to our experiments ( $r \approx 30 \text{ \AA}$ ), the highest peaks encountered have similar intensity values (slightly below 200 or -200), whatever  $r$ . The transition observed at  $15 \text{ \AA}$  is indicative of the nanometer scale of the structural coherence in the material, in

agreement with  $L_a$  and  $L_c$  values obtained from X-ray diffraction. The constant width envelope of  $r^2G(r)$  from 15 to 30 Å nevertheless indicates that some structural coherence still remains between atoms having those interatomic distances.

Comparing now  $r^2G(r)$  of PyC-2 to the one of PyC-1 we see that a left arrow shaped envelope also develops until around 15 Å, yet with lower amplitude (the highest peak having an amplitude of around 150 in that case). However, above 15 Å, the amplitude of the highest peaks diminishes regularly with  $r$  (right arrow shaped envelope), giving to  $r^2G(r)$  the envelope of a lozenge centered on 15 Å. This behavior is typical of a progressive and complete loss of structural coherence between atoms having interatomic distances above 15 Å. Indeed, as can be seen on Figure 9d, almost no correlation is found for atoms distant of 30 Å in PyC-2. An extra discussion on the envelopes of the  $r^2G(r)$  data is provided as supporting information.

We note that information before 15 Å does not allow for a clear distinction between those structures, indicating that there are only slight differences in the short-range neighborhoods of those two materials.

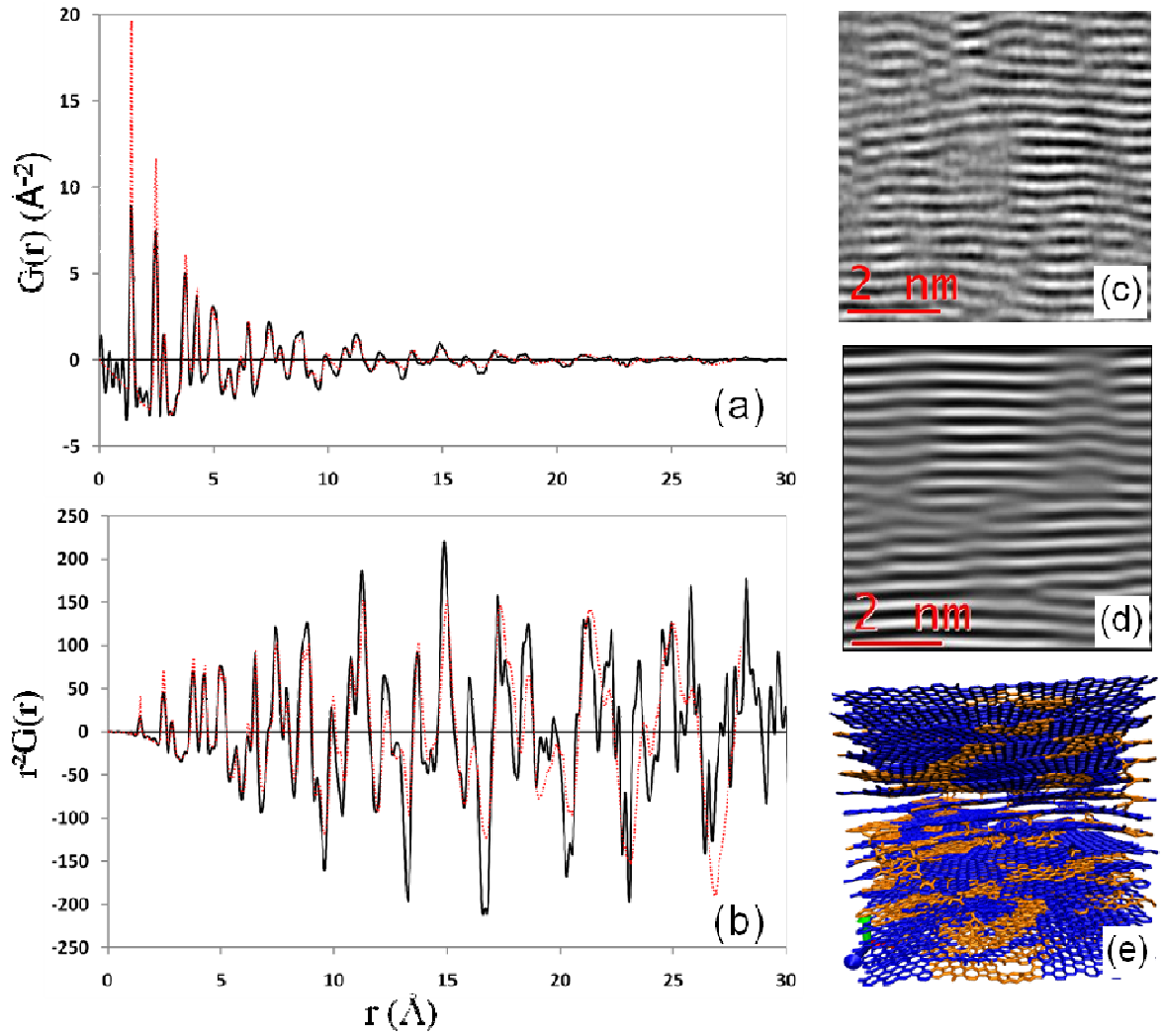


Figure 10: Comparison of the experimental PDF data of PyC-1 (black solid line) with those of an atomistic model of an RL PyC (dashed line) taken from ref [49]; a:  $G(r)$ , b:  $r^2G(r)$ , c: HRTEM image of PyC-1 (enlargement of Fig. 5 [Z3]), d: simulated HRTEM image of the model, and e: Snapshot of the model (pure hexagonal domains are shown with blue bonds, defect containing domains with orange bonds).

We now compare the PDF of our rough laminar pyrocarbon (PyC-1) to the one of an atomistic PyC model reconstructed from the HRTEM image of an RL PyC matrix of a C/C composite using the IGAR simulation method [49]. Figure 10a shows the  $G(r)$  function of PyC-1 together with the one of the model; the corresponding  $r^2G(r)$  functions are given on Fig. 10b. HRTEM images of the two nanotextures are given on Fig. 10c (PyC-1) and Fig. 10d

(simulated from the atomistic model using the multislice code NCEMSS [62]). A snapshot of the model is also given on Fig. 10e. As can be seen on Figs 10a and 10b, all the pyrocarbon peaks are well reproduced by the model, although the first four peaks from the model are a bit thinner than their experimental counterparts, possibly because of a too rigid interaction potential. Also, the global “left arrow with large tail” envelope of  $r^2G(r)$  is particularly well reproduced by the model. On a microscopic perspective, we can see on Fig. 10e that the atomistic structure of the model is made of purely hexagonal domains (blue) connected together by screw dislocations and some disordered regions (orange) essentially made of pentagons and heptagons (around 5-6 % each). This nanostructure is clearly richer than the simple graphitic cylindrical crystallites given by the sole knowledge of  $L_a$ ,  $L_c$ , and  $d_{002}$ . Unfortunately, the 3D HRTEM-like image synthesis, a necessary step in the IGAR approach, requires materials having highly anisotropic HRTEM images, preventing so far the construction of atomistic models for smooth laminar pyrocarbons like PyC-2. Last but not least, the low hydrogen content of our PyCs was confirmed quantitatively by the neutron diffraction pattern; indeed hydrogen has a large incoherent scattering cross-section which should increase significantly the background signal, even with only a few atomic percent. It was not the case in our experiments. From the point of view of structural modeling, our experience in preparing hydrogenated pyrocarbons by the IGAR method with 5% at. hydrogen has led to structures with a high density of “graphane” sites, indicating that 5% at. is probably an excessively large amount for insertion in defective zones.

#### 4. Conclusions

Thin foils of two distinct pyrocarbons, belonging to the RL and SL families were characterized by density measurements, Raman spectrometry, X-ray diffraction and

HRTEM/SAED observations. For the first time, we have provided PDF data from neutron diffraction experiments for these materials. While  $G(r)$  functions did not allow to discriminate properly between those two materials, comparing the  $r^2G(r)$  curves after 15 Å shows unambiguous differences in long-distance correlation, SL becoming quicker uncorrelated than RL; this is in agreement with  $L_a$  and  $L_c$  values from X-ray diffraction data. A striking fact is that SL and RL are known to differ on a large-scale criterion (i.e. the optical light anisotropy) but also – as confirmed by this work – by their arrangement at the 2 nm scale.

The PDF data of RL PyC has been compared to similar data obtained from an image-guided atomistic reconstruction (IGAR) method of an RL PyC, showing excellent agreement in the long-distance part. This provides also a validation of the accuracy of the reconstructed model, confirming the pertinence of the HRTEM image-guided reconstruction method, which had already been illustrated by the comparison of HRTEM images obtained from the model [62] and experimental images [49].

This study confirms the interest of PDF data in describing the nanotexture of pyrocarbons, even though they only give orientation-averaged information about intrinsically anisotropic materials. Further work is to enrich the IGAR method by adding constraints arising from the PDF data, in a reverse Monte Carlo spirit, and produce models for SL PyC. On the experimental point, pyrocarbons with nanotextures other than SL and RL, i.e., ReL, G, and DL, have to be investigated and systematically compared to the previous ones; this will help building a more complete portrait of these materials. Eventually, the materials investigated in this work appear to have much lower hydrogen content than previously thought. This point probably also deserves further investigations.

## **Acknowledgements**

ANR is acknowledged for funding M.L. post-doc under grant # ANR 2010 BLAN 0929 01 for the project “PyroMaN: Pyrocarbon Matrices Nanotextures”, with support from the Aerospace Valley Foundation. A. Delcamp and S. Bertrand from Snecma Propulsion Solide are acknowledged for their help in sample preparation, G. Chollon and C François for advices on the samples elaboration and characterization, D. Rembelski for his contribution during a training period. H. Guegan (CENBG Gradignan) and B.Boyer (Géosciences Montpellier) are also acknowledged for respectively ERDA analyses and SIMS characterizations.

## **References**

- [1] Manocha LM, Fitzer E. Carbon reinforcements and C/C composites. 1st ed. Berlin: Springer ; 1998.
  
- [2] Lachaud J,Vignoles GL, Goyhénèche J-M, Epherre J-F. Ablation in carbon/carbon composites: microscopic observations and 3D numerical simulation of surface roughness. Ceram. Trans. 2005; 191(1):149-160.
  
- [3] Filipuzzi L, Subrenat E. Thermostructural composites and nuclear fusion, Industrial Ceramics 1998; 18(2):103-8
  
- [4] Awasthi S, Wood JL. Carbon-carbon composite materials for aircraft brakes, Ceram. Eng. Sci. Procs. 1988; 9(7-8):553-60.
  
- [5] Naslain R. Design, preparation and properties of non-oxide CMCs for application in engines and nuclear reactors: An overview. Compos. Sci. Technol. 2004; 64(2):155-70.

- [6] Delhaès P. Chemical vapor deposition and infiltration processes of carbon materials, Carbon 2002 ; 40(5) :641-57
- [7] Bourrat X, Lavenac J, Langlais F, Naslain R. The role of pentagons in the growth of laminar pyrocarbon. Carbon 2001; 39(15):2376-80.
- [8] Dong GL, Hüttinger KJ. Consideration of reaction mechanisms leading to pyrolytic carbon of different textures. Carbon 2002; 40(14):2515-2528.
- [9] Lavenac J, Langlais F, Bourrat X, Naslain R. Deposition process of laminar pyrocarbon from propane. J. Phys. IV 2001 ; 11(Pr3) :1013-21.
- [10] Lieberman ML, Pierson HO. Effect of Gas Phase Conditions on Resultant Matrix Pyrocarbons in Carbon/Carbon Composites. Carbon 1974; 12(3):233-41.
- [11] Le Poche H, Bourrat X, Dourges M-A, Vignoles GL, Langlais F. Influence of the gas-phase maturation on the CVD/CVI process and the micro-texture of laminar pyrocarbon from propane, Procs High-Temperature Ceramic Matrix Composites 5, Seattle (WA, USA): The American Ceramic Society, 2005; p. 81-6.
- [12] De Pauw V, Reznik B, Kalhöfer S, Gerthsen D, Hu ZJ, Hüttinger KJ. Texture and nanostructure of pyrocarbon layers deposited on planar substrates in a hot-wall reactor. Carbon. 2003;41(1):71-7.
- [13] Harris PJF. New Perspectives on the structure of Graphitic Carbons. Critical Review in Solid State and Materials Science 2005; 30(4):235-53.
- [14] Oberlin A. Pyrocarbons. Carbon. 2002;40(1):7-24.

- [15] Rouzaud JN, Clinard C. Quantitative high-resolution transmission electron microscopy: a promising tool for carbon materials characterization. *Fuel Processing Technology* 2002; 77–78:229–35.
- [16] Bourrat X. Pyrocarbon anisotropy as measured by electron diffraction and polarized light. *J Mater Res* 2000; 15(1):92–101.
- [17] Reznik B, Gerthsen D, Hüttinger KJ. Micro- and nanostructure of the carbon matrix of infiltrated carbon fiber felts. *Carbon*. 2001;39(2):215-29.
- [18] Reznik B, Hüttinger KJ. On the Terminology for pyrolytic carbon. *Carbon* 2002; 40(4):617-36.
- [19] Warren BE. X - Ray Diffraction Study of Carbon Black. *J Chem. Phys.* 1934; 2(9):551-5.
- [20] Rouzaud J-N, Oberlin A, Beny-Bassez C. Carbon films: Structure and microtexture (optical and electron microscopy, Raman spectroscopy). *Thin Solid Films* 1983; 105(1):75-96.
- [21] Knight DS, White WB. Characterization of diamond films by Raman spectroscopy. *J Mater Res.* 1989;4(2):385-93.
- [22] Vallerot J-M, Bourrat X, Mouchon A, Chollon G. Quantitative structural and textural assessment of laminar pyrocarbons through Raman spectroscopy, electron diffraction and few other techniques. *Carbon* 2006; 44(9):1833-44.
- [23] Bourrat X, Langlais F, Chollon G, Vignoles GL, Low Temperature Pyrocarbon : a review, *J. Braz. Chem. Soc.* 2006; 117(6):1090-5.

- [24] Bourrat X, Fillion A, Naslain R, Chollon G, Brendlé M. Regenerative laminar pyrocarbon, *Carbon* 2002; 40(15):2931–45.
- [25] Biscoe J, Warren BE. An X-ray study of carbon black. *J App. Phys.* 1942; 13(6):364-71.
- [26] Ruland W. X-ray studies of Graphitic Carbons. *Acta Cryst.* 1965; 18(6):992-6.
- [27] Ergun S. Analysis of coherence, strain, thermal vibration and preferred orientation in carbons by X-ray diffraction. *Carbon* 1976; 14(3):139-50.
- [28] Franklin RE. The Structure of Graphitic Carbons. *Acta Cryst.* 1951; 4(3):253-61.
- [29] Yang D, Frindt R. Powder X-ray diffraction of turbostratically stacked layer systems. *J. Mater. Res.* 1996;11(7):1733–8.
- [30] Egami T, Billinge SJL. *Underneath the Bragg Peaks: Structural Analysis of Complex materials.* Oxford: Pergamon Press, 2003.
- [31] Warren BE. X-ray diffraction in random layer lattices. *Physical Review.* 1941;59(9):693-8.
- [32] Franklin R. E.. The interpretation of Diffuse X-ray Diagrams of Carbon. *Acta Cryst.* 1950; 3(2):107-21.
- [33] Petkov V, Difrancesco RG, Billinge SJL, Acharya M, Foley HC. Local structure of nanoporous carbons. *Philos. Mag. B* 1999;79(10):1519-30.
- [34] Papanek, P, Kamitakahara WA, Zhou P, Fischer JE. Neutron scattering studies of disordered carbon anode materials. *J. Phys.:Cond. Mat.* 2001; 13(36):8287-301

- [35] Oshida K, Nakazawa T, Osawa K, Endo M, Nano structure of low crystallinity carbon materials analyzed by using high energy X-ray diffraction. *Cent. Eur. J. Phys.* 2009; 7(2):232-6.
- [36] Szczygielska A, Burian A, Duber S, Dore JC, Honkimäki V. Radial distribution function analysis of the graphitization process in carbon materials. *J. Alloys Compounds.* 2001;328(1-2):231-6.
- [37] Szczygielska A, Burian A, Dore JC, Honkimäki V, Duber S. Local structure of saccharose- and anthracene-based carbons studied by wide-angle high-energy X-ray scattering. *J. Alloys Compounds.* 2004;362(1-2):307-13.
- [38] Pikunic J, Gubbins KE, Pellenq RJ-M, Cohaut N, Rannou I, Guet J-M, Clinard C, Rouzaud J-N. Realistic molecular models for saccharose-based carbons. *App. Surf. Sci.* 2001; 196(1):98-104.
- [39] Palmer JC, Brennan JK, Hurley MM, Balboa A, Gubbins KE, Detailed structural models for activated carbons from molecular simulation. *Carbon* 2009; 47(12):2904-13.
- [40] Zetterström P, Urbonaitė S, Lindberg F, Delaplane RG, Leis J, Svensson G, Reverse Monte Carlo studies of nanoporous carbon from TiC. *J. Phys.: Condens. Matter* 2005; 17(23):3509-24.
- [41] Burian A, Dore, J. C., Fischer, H. E., Sloan, J. Structural studies of multiwall carbon nanotubes by neutron diffraction. *Phys. Rev. B* 1999; 59(3):1665-8.
- [42] Burian A, Dore JC, Hannon AC, Honkimäki V. Complementary studies of structural characteristics for carbon materials with X-rays and neutrons. *J Alloys Compounds.* 2005;401(1-2):18-23.

- [43] O'Malley B, Snook I. Reverse Monte Carlo analysis of the structure of glassy carbon using electron-microscopy data. *Phys. Rev. B.* 1998; 57(22):14148–57.
- [44] Petersen T, Yarovsky I, Snook I, McCulloch DG, Opletal G. Microstructure of an industrial char by diffraction techniques and Reverse Monte Carlo modeling. *Carbon* 2004; 42(12-13):2457-69.
- [45] McGreevy RL, Pusztai L. Reverse Monte Carlo simulation: A new technique for the determination of disordered structures. *Mol. Sim.* 1988;1(6):359–67.
- [46] T. Petersen, I. Yarovsky, I. Snook, D. G. McCulloch, G. Opletal, Structural analysis of carbonaceous solids using an adapted reverse Monte Carlo algorithm, *Carbon* 2003; 41(12):2403-11.
- [47] Pikunic J, Clinard C, Cohaut N, Gubbins KE, Guet J-M, Pellenq RJ-M, Rannou I, Rouzaud J-N, Structural Modeling of Porous Carbons: Constrained Reverse Monte Carlo Method, *Langmuir* 2003; 19(20):8565-82.
- [48] Jain SK, Pellenq RJ-M, Pikunic JP, Gubbins KE. Molecular Modeling of Porous Carbons Using the Hybrid Reverse Monte Carlo Method. *Langmuir* 2006; 22(24):9942–8.
- [49] Leyssale JM, Da Costa JP, Germain C, Weisbecker P, Vignoles GL. An image-guided atomistic reconstruction of pyrolytic carbons. *Appl. Phys. Lett.* 2009; 95(23):231912.
- [50] Iwashita N, Park CR, Fujimoto H, Shiraishi M, Inagaki M. Specification for a standard procedure of X-ray diffraction measurements on carbon materials. *Carbon* 2004; 42(4):701-14.
- [51] Diffra<sup>plus</sup> TOPAS (Total Pattern Analysis Solution) Software, distributed by Bruker AXS. <http://www.bruker-axs.com/topas.html>

- [52] Fischer HE, Cuello CJ, Palleau P, Feltin D, Barnes AC, Badyal YS, Simonson JM. D4c: A very high precision diffractometer for disordered materials. *App. Phys. A.* 2002; 74:S160-2.
- [53] Fischer HE, Barnes AC, Salmon PS. Neutron and x-ray diffraction studies of liquids and glasses. *Reports on Progress in Physics.* 2006;69(1):233-99.
- [54] Drits VA, Tchoubar C. X-ray diffraction by disordered lamellar structures. Chapter 7. *Structural Characteristics of Carbons.* Berlin, Heidelberg, New York: Springer-Verlag, 1990:233-303.
- [55] Fujimoto H.. Theoretical X-ray Scattering intensity of carbons with turbostratic stacking and AB stacking structures. *Carbon* 2003; 41(8):1585-92.
- [56] Li ZQ, Lu CJ, Xia ZP, Zhou Y, Luo Z, X-ray diffraction patterns of graphite and turbostratic carbon, *Carbon* 2007; 45(8):1686-95
- [57] Mitchell D. R. G. Script to compute the average background subtracted filter images. v1.3, February 2007. URL: [http://www.dmscripting.com/hrtem\\_filter.html](http://www.dmscripting.com/hrtem_filter.html)
- [58] Kilaas R. Optimal and near-optimal filters in high-resolution electron microscopy *J. Microscopy*, 1998; 190(1-2):45-51.
- [59] Reznik B, Gerthsen D. Microscopic study of failure mechanisms in infiltrated carbon fiber felts, *Carbon* 2003; 41(1):57-69.
- [60] Chen TF, Reznik B, Gerthsen D, Zhan WG, Hüttinger KJ, Microscopical study of carbon/carbon composites obtained by chemical vapor infiltration of 0°/0°/90°/90° carbon fiber preforms, *Carbon* 2005; 43(15): 3088-98.

[61] Zhang WG, Hüttinger KJ. Densification of a 2D carbon fiber preform by isothermal, isobaric CVI: Kinetics and carbon microstructure. *Carbon*. 2003;41(12):2325-37.

[62] Kilaas R. Interactive software for simulation of high resolution TEM images. Proceedings 22<sup>nd</sup> Annual conference of the Microbeam Analysis Society. Kona, Hawaii (1987), pp. 293-300.